

Associating High-Dimensional Longitudinal Datasets through an Efficient Cross-Covariance Decomposition

Jianbin Tan^{*}

Department of Biostatistics and Bioinformatics, Duke University, Durham,
NC, U.S.A.
and
Pixu Shi[†]

Department of Biostatistics and Bioinformatics, Duke University, Durham,
NC, U.S.A.

Abstract

Understanding associations between paired high-dimensional longitudinal datasets is a fundamental yet challenging problem that arises across scientific domains, including longitudinal multi-omic studies. The difficulty stems from the complex, time-varying cross-covariance structure coupled with high dimensionality, which complicates both model formulation and statistical estimation. To address these challenges, we propose a new framework, termed Functional-Aggregated Cross-covariance Decomposition (FACD), tailored for canonical cross-covariance analysis between paired high-dimensional longitudinal datasets through a statistically efficient and theoretically grounded procedure. Unlike existing methods that are often limited to low-dimensional data or rely on explicit parametric modeling of temporal dynamics, FACD adaptively learns temporal structure by aggregating signals across features and naturally accommodates variable selection to identify the most relevant features associated across datasets. We establish statistical guarantees for FACD and demonstrate its advantages over existing approaches through extensive simulation studies. Finally, we apply FACD to a longitudinal multi-omic human study, revealing blood molecules with time-varying associations across omic layers during acute exercise.

KEYWORDS: *Canonical correlation analysis; high-dimensional functional data; longitudinal multi-omic data; operator decomposition; sparse singular value decomposition*

^{*}Email: jianbin.tan@duke.edu

[†]Email: pixu.shi@duke.edu

1 Introduction

Understanding associations between paired high-dimensional longitudinal datasets is increasingly important in biology and medicine. The growing availability of longitudinal multi-omic studies, which collect multiple types of high-dimensional molecular data over time, enables the investigation of dynamic processes across molecular layers such as the metabolome, microbiome, lipidome, proteome, and transcriptome. Analyses of such data have uncovered valuable insights into temporal adaptations and coordinated molecular activities during disease progression and in response to external stimuli. Notable examples include monitoring of inflammatory bowel disease (Ng et al., 2023) and prediabetes (Zhou et al., 2019), the progression of COVID-19 infection (Diray-Arce et al., 2023), physiological responses to acute exercise (Contrepois et al., 2020; MoTrPAC Study Group Primary authors et al., 2024), and exposure to environmental stressors such as high altitude (Han et al., 2024) or short-term spaceflight (Tierney et al., 2024). However, these datasets are often characterized by high dimensionality, irregular and sparse time sampling, and complex temporal patterns, making it challenging to extract interpretable, time-varying associations between paired data modalities.

In cross-sectional settings, canonical correlation analysis (CCA) is a classical tool for identifying associations between paired datasets by seeking linear projections that maximize their correlation (Härdle et al., 2015). CCA has been extended in many directions, including to high-dimensional settings (Witten and Tibshirani, 2009; Parkhomenko et al., 2009; Lin et al., 2013) and to functional/longitudinal data (Shin and Lee, 2015; Górecki et al., 2017; Hao et al., 2017; Górecki et al., 2020; Lee et al., 2023). Nevertheless, extending CCA to data that are both high-dimensional and functional/longitudinal is far from straightforward. Existing CCA methods for multivariate functional or longitudinal data (Shin and Lee, 2015; Górecki et al., 2017; Lee et al., 2023) are mainly developed for low-dimensional regimes and may not scale well to modern high-dimensional studies. Moreover, many of these approaches impose pre-specified parametric models for temporal structure, which can limit flexibility and robustness in real-world applications where dynamics are complex and not well captured by restrictive parametric forms.

To accommodate richer temporal patterns in infinite-dimensional spaces, additional assumptions are needed to address the non-invertibility issue in CCA, as discussed in [He et al. \(2003\)](#); [Eubank and Hsing \(2008\)](#); [Hsing and Eubank \(2015\)](#). Alternative strategies instead explore associations through cross-covariance-based approaches. For example, functional singular component analysis associates between univariate functional features ([Yang et al., 2011](#)) and functional partial least squares links between univariate and multivariate functional data ([Beyaztas and Shang, 2020](#)). However, direct extension of these methods to two high-dimensional longitudinal datasets is highly nontrivial. Most existing approaches ([Eubank and Hsing, 2008](#); [Yang et al., 2011](#); [Hsing and Eubank, 2015](#)) rely on a singular value decomposition (SVD) of correlation or cross-covariance operators estimated from empirical data. In the high-dimensional longitudinal regime, such an SVD requires factorizing operators between high-dimensional functional spaces, which is practically intractable and statistically inefficient, and often requires large sample sizes.

To address the above challenges, we propose a novel framework, **Functional-Aggregated Cross-covariance Decomposition (FACD)**, tailored to factorizing high-dimensional cross-covariance operators for functional/longitudinal data. Building on ideas similar to CCA, FACD aims to maximize the cross-covariance between high-dimensional functional/longitudinal datasets through joint, time-dependent dimension reduction of the two datasets, as illustrated in Figure 1. We first show that extracting canonical cross-covariance components can be formulated as a spectral decomposition of the cross-covariance operator, which in turn admits a representation via functional basis expansion. Rather than relying on pre-specified bases, we introduce a functional aggregation technique that utilizes the cross-covariance structure to construct data-adaptive bases. These bases account for shared patterns across high-dimensional features to represent their cross-covariance efficiently, providing greater flexibility for capturing temporal patterns in real-world longitudinal data.

Leveraging the relationship between data-adaptive bases and the decomposition of the cross-covariance, FACD avoids direct spectral decomposition of high-dimensional operators by transforming the problem into a matrix SVD, yielding a practically tractable and statistically efficient implementation. To improve interpretability in high dimensions, we further incorporate sparsity into the FACD procedure, enabling the selection of key features across

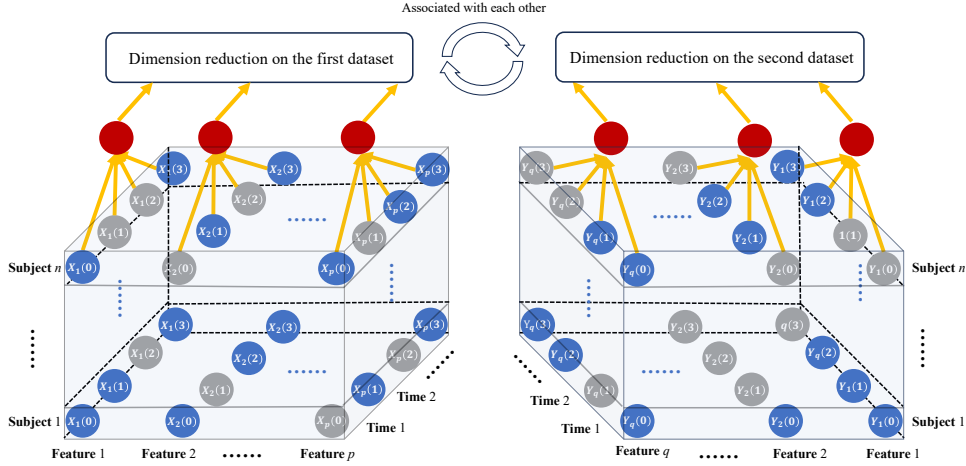


Figure 1: Diagram illustrating longitudinal associations between two high-dimensional longitudinal datasets. Each dataset is represented by an array indexed by feature, time and subject. Yellow arrows indicate functional loadings that aggregate features in a time-dependent manner, red circles denote aggregated features whose cross-covariance between datasets is maximized, and missing observations at certain time points are shown in gray.

datasets. These procedures accommodate irregular and sparse time observations, making FACD applicable to a wide range of longitudinal settings.

We provide theoretical support and statistical guarantees for the FACD framework. Through extensive simulation studies, we demonstrate the superior performance of FACD compared to related methods in recovering canonical components. Finally, we apply FACD to a longitudinal multi-omic study profiling blood molecules in healthy human subjects undergoing acute physical exercise (Contreipois et al., 2020). The analysis reveals meaningful temporal associations, at both the global and molecular levels, across omic layers, underscoring the potential of FACD to advance our scientific understanding of dynamic biological interactions.

The rest of this article is organized as follows. In Section 2, we introduce the basic theoretical framework of FACD for high-dimensional functional data. We describe the implementation of FACD for observed longitudinal data in Section 3 and provide its statistical guarantee in Section 4. We conduct simulation studies to evaluate the effectiveness of FACD in Section 5 and apply FACD to real-world data in Section 6. Finally, we conclude with a discussion in Section 7. Additional supporting results are provided in the Supplementary Materials.

2 Functional-Aggregated Cross-covariance Decomposition

We first introduce notations for Hilbert spaces of functions and their associated operators. For $\mathbf{f}(t), \mathbf{g}(t) \in \mathbb{R}^p$ with $t \in \mathcal{T}$, define the inner product $\langle \mathbf{f}, \mathbf{g} \rangle_p := \int_{\mathcal{T}} \mathbf{f}(t)^\top \mathbf{g}(t) w(dt)$, where w is a probability measure on \mathcal{T} . Without loss of generality, we set $\mathcal{T} = [0, 1]$ and take w as the Lebesgue measure. Let $L^2(\mathbb{R}^p)$ denote the Hilbert space of square-integrable functions on \mathcal{T} valued in \mathbb{R}^p , equipped with inner product $\langle \cdot, \cdot \rangle_p$ and norm $\|\cdot\|_p := \sqrt{\langle \cdot, \cdot \rangle_p}$. When $p = 1$, we simplify $\|\cdot\|_p$ to $\|\cdot\|$. We also use $\|\cdot\|$ to denote the Euclidean norm for real vectors. Let $\|\cdot\|_F$ be the Frobenius norm of a matrix, and write $\text{span}\{f_1, f_2, \dots\}$ for the closure of the functional space spanned by $\{f_1, f_2, \dots\}$. Define $\mathbb{I}(\cdot)$ as the indicator function.

Define the norm $\|\mathcal{A}\|_\infty := \sup_{\{\mathbf{f} \in L^2(\mathbb{R}^p); \|\mathbf{f}\|_p \leq 1\}} \|\mathcal{A}\mathbf{f}\|_q$ for an operator \mathcal{A} mapping from $L^2(\mathbb{R}^p)$ to $L^2(\mathbb{R}^q)$. For a kernel function $\mathbf{K}(t_1, t_2) \in \mathbb{R}^{p \times q}$, define its associated integral operator \mathcal{K} from $L^2(\mathbb{R}^q)$ to $L^2(\mathbb{R}^p)$ by $(\mathcal{K}\mathbf{f})(t_1) = \int_{\mathcal{T}} \mathbf{K}(t_1, t_2) \mathbf{f}(t_2) dt_2, \quad t_1 \in \mathcal{T}, \forall \mathbf{f} \in L^2(\mathbb{R}^q)$. We say that \mathcal{A} is compact if there exist $\lambda_1 \geq \lambda_2 \geq \dots \geq 0$ and orthonormal functions $\{\mathbf{f}_r \in L^2(\mathbb{R}^p); r \geq 1\}$ and $\{\mathbf{g}_r \in L^2(\mathbb{R}^q); r \geq 1\}$ such that $\lim_{R \rightarrow \infty} \left\| \mathcal{A} - \sum_{r=1}^R \lambda_r \mathbf{f}_r \otimes \mathbf{g}_r \right\|_\infty = 0$, where \otimes denotes the tensor product, defining an operator $\mathbf{f}_r \otimes \mathbf{g}_r$ by $(\mathbf{f}_r \otimes \mathbf{g}_r)\mathbf{h} = \mathbf{g}_r \langle \mathbf{f}_r, \mathbf{h} \rangle_p$ for all $\mathbf{h} \in L^2(\mathbb{R}^p)$. If \mathcal{A} is an infinite-dimensional compact operator, we write $\mathcal{A} = \sum_{r=1}^\infty \lambda_r \mathbf{f}_r \otimes \mathbf{g}_r$, where λ_r is the r th singular value and $\mathbf{f}_r, \mathbf{g}_r$ are the corresponding singular functions. See Section 4.3 of [Hsing and Eubank \(2015\)](#) for details.

2.1 Canonical Cross-Covariance between Functional Data

Let $\mathbf{X}(t) = (X_1(t), \dots, X_p(t))^\top$ denote a p -dimensional random function representing the values of p features at time t , where $t \in \mathcal{T}$. Similarly, let $\mathbf{Y}(s) \in \mathbb{R}^q$ for $s \in \mathcal{S}$ denote a second data source. For simplicity, we assume $\mathcal{T} = \mathcal{S} = [0, 1]$, though our method also applies when \mathcal{T} and \mathcal{S} are different intervals. We define the covariance and cross-covariance functions as $\mathbf{R}_X(t_1, t_2) := \text{Cov}\{\mathbf{X}(t_1), \mathbf{X}(t_2)\} \in \mathbb{R}^{p \times p}$, $\mathbf{R}_Y(t_1, t_2) := \text{Cov}\{\mathbf{Y}(t_1), \mathbf{Y}(t_2)\} \in \mathbb{R}^{q \times q}$, and $\mathbf{R}_{XY}(t_1, t_2) := \text{Cov}\{\mathbf{X}(t_1), \mathbf{Y}(t_2)\} \in \mathbb{R}^{p \times q}$ for $t_1, t_2 \in \mathcal{T}$. The corresponding integral operators are denoted by \mathcal{R}_X , \mathcal{R}_Y , and \mathcal{R}_{XY} .

To capture the temporal connections between \mathbf{X} and \mathbf{Y} , we consider

$$\{\tilde{\mathbf{A}}_X, \tilde{\mathbf{A}}_Y\} = \arg \max_{\mathbf{A}_X \in \mathbb{S}_p, \mathbf{A}_Y \in \mathbb{S}_q} \text{Cov}^2 \left(\int_0^1 \mathbf{A}_X^\top(t) \mathbf{X}(t) dt, \int_0^1 \mathbf{A}_Y^\top(t) \mathbf{Y}(t) dt \right), \quad (1)$$

where \mathbb{S}_p and \mathbb{S}_q denote the unit spheres in $L^2(\mathbb{R}^p)$ and $L^2(\mathbb{R}^q)$, ensuring the optimization is well-posed and scale-invariant. Here, $\tilde{\mathbf{A}}_X$ and $\tilde{\mathbf{A}}_Y$ are functional loadings representing the time-varying contributions of each feature to the dominant association between \mathbf{X} and \mathbf{Y} .

Since (1) is defined based on the cross-covariance, we refer to it as canonical cross-covariance analysis. Canonical cross-covariance analysis is commonly used as a substitute for CCA in high-dimensional settings (Witten and Tibshirani, 2009; Parkhomenko et al., 2009; Lin et al., 2013), where the empirical variance matrices are often not invertible, making CCA inapplicable. In the high-dimensional functional data setting, CCA not only faces non-invertibility issues in empirical matrices, but its theoretical solution may also fail to exist due to the infinite dimensionality of functional data (see Part A.1 of the Supplementary Materials). In contrast, we show below that the canonical cross-covariance solution between \mathbf{X} and \mathbf{Y} always exists under mild conditions.

Theorem 1. *Assume that $\mathbf{R}_{XY}(t_1, t_2)$ is continuous with respect to t_1 and t_2 . Then, \mathcal{R}_{XY} is a compact operator with the following decomposition:*

$$\mathcal{R}_{XY} = \sum_{r=1}^{\infty} \lambda_r \tilde{\mathbf{A}}_r^X \otimes \tilde{\mathbf{A}}_r^Y \text{ or equivalently, } \mathbf{R}_{XY}(t_1, t_2) = \sum_{r=1}^{\infty} \lambda_r \tilde{\mathbf{A}}_r^X(t_1) \{\tilde{\mathbf{A}}_r^Y(t_2)\}^\top, \quad (2)$$

where $\lambda_1 \geq \lambda_2 \geq \dots \geq 0$ are the singular values, and $\tilde{\mathbf{A}}_r^X$ and $\tilde{\mathbf{A}}_r^Y$ are singular functions, respectively. In addition,

$$\max_{\mathbf{A}_X \in \mathbb{S}_p, \mathbf{A}_Y \in \mathbb{S}_q} \text{Cov}^2 \left(\int_0^1 \mathbf{A}_X^\top(t) \mathbf{X}(t) dt, \int_0^1 \mathbf{A}_Y^\top(t) \mathbf{Y}(t) dt \right) = \lambda_1^2,$$

where the maximum is attained at $\mathbf{A}_X = \pm \tilde{\mathbf{A}}_1^X$ and $\mathbf{A}_Y = \pm \tilde{\mathbf{A}}_1^Y$.

Theorem 1 demonstrates that (1) can be solved by the decomposition of the cross-covariance operator \mathcal{R}_{XY} . This decomposition can be considered an infinite-dimensional extension of the SVD from matrices to compact cross-covariance operators, where $\tilde{\mathbf{A}}_1^X, \tilde{\mathbf{A}}_1^Y$,

and λ_1 are referred to as the first canonical functional loadings and the first cross-covariance, respectively. The r th canonical functional loadings and cross-covariance can be defined similarly using the r th component in (2).

Under the above setting, we define the r th canonical scores for \mathbf{X} and \mathbf{Y} by

$$z_r^X := \int_0^1 \{\tilde{\mathbf{A}}_r^X(t)\}^\top \{\mathbf{X}(t) - \boldsymbol{\mu}_X(t)\} dt, \quad z_r^Y = \int_0^1 \{\tilde{\mathbf{A}}_r^Y(t)\}^\top \{\mathbf{Y}(t) - \boldsymbol{\mu}_Y(t)\} dt, \quad (3)$$

where $\boldsymbol{\mu}_X$ and $\boldsymbol{\mu}_Y$ are the mean functions of \mathbf{X} and \mathbf{Y} , respectively. This pair of random variables captures the overall dependency between \mathbf{X} and \mathbf{Y} by aggregating information across both time and features, with the contributions weighted by the functional loadings $\tilde{\mathbf{A}}_r^X$ and $\tilde{\mathbf{A}}_r^Y$. It can be shown that $\mathbb{E}z_r^X = 0$, $\mathbb{E}z_r^Y = 0$ and $\mathbb{E}z_{r_1}^X z_{r_2}^Y = \lambda_{r_1} \mathbb{I}(r_1 = r_2)$.

Remark 1 (Challenges of Canonical Cross-Covariance Analysis in High Dimensions). *In order to obtain $\tilde{\mathbf{A}}_r^X$ and $\tilde{\mathbf{A}}_r^Y$ based on the cross-covariance decomposition in Theorem 1, one approach is to perform spectral decompositions of the kernels $\mathbf{L}_X(t_1, t_2) := \int_0^1 \mathbf{R}_{XY}(t_1, t) \mathbf{R}_{XY}^\top(t_2, t) dt = \sum_{r=1}^{\infty} \lambda_r^2 \tilde{\mathbf{A}}_r^X(t_1) \{\tilde{\mathbf{A}}_r^X(t_2)\}^\top \in \mathbb{R}^{p \times p}$ and $\mathbf{L}_Y(t_1, t_2) := \int_0^1 \mathbf{R}_{XY}^\top(t, t_1) \mathbf{R}_{XY}(t, t_2) dt = \sum_{r=1}^{\infty} \lambda_r^2 \tilde{\mathbf{A}}_r^Y(t_1) \{\tilde{\mathbf{A}}_r^Y(t_2)\}^\top \in \mathbb{R}^{q \times q}$, where λ_r^2 is the r th eigenvalue of \mathbf{L}_X and \mathbf{L}_Y , with $\tilde{\mathbf{A}}_r^X$ and $\tilde{\mathbf{A}}_r^Y$ being the corresponding eigenfunctions. However, the spectral decompositions of $\mathbf{L}_X(t_1, t_2)$ and $\mathbf{L}_Y(t_1, t_2)$ are impractical when p and q are large, as they involve high-dimensional eigenfunction computation from the complicated kernels.*

2.2 Functional-Aggregated Decomposition of Cross-Covariances

In this subsection, we propose an approximation of the singular functions $\tilde{\mathbf{A}}_r^X$ and $\tilde{\mathbf{A}}_r^Y$ that avoids high-dimensional kernel spectral decomposition, which can leverage the high-dimensional feature structure of the data to obtain an efficient representation. We begin by presenting the following theorem.

Theorem 2 (Basis Expansion of Cross-Covariance). *Under conditions in Theorem 1, define $\mathcal{H}_1 := \text{span}\{\tilde{A}_{rj}^X; j = 1, \dots, p, r \geq 1\} \subset L^2(\mathbb{R})$ and $\mathcal{H}_2 := \text{span}\{\tilde{A}_{rm}^Y; m = 1, \dots, q, r \geq 1\} \subset L^2(\mathbb{R})$, where $(\tilde{A}_{r1}^X, \dots, \tilde{A}_{rp}^X) = \tilde{\mathbf{A}}_r^X$ and $(\tilde{A}_{r1}^Y, \dots, \tilde{A}_{rq}^Y) = \tilde{\mathbf{A}}_r^Y$. Then for any complete orthonormal bases $\{\psi_{k_1}^X; k_1 \geq 1\}$ and $\{\psi_{k_2}^Y; k_2 \geq 1\}$ in $L^2(\mathcal{T})$ such that $\mathcal{H}_1 \subset \text{span}\{\psi_{k_1}^X, k_1 \geq 1\}$ and $\mathcal{H}_2 \subset \text{span}\{\psi_{k_2}^Y, k_2 \geq 1\}$, we have*

1} and $\mathcal{H}_2 \subset \text{span}\{\psi_{k_2}^Y, k_2 \geq 1\}$,

$$\mathbf{R}_{XY}(t_1, t_2) = \sum_{k_1=1}^{\infty} \sum_{k_2=1}^{\infty} \Lambda_{k_1, k_2}^{XY} \psi_{k_1}^X(t_1) \psi_{k_2}^Y(t_2),$$

where $\Lambda_{k_1, k_2}^{XY} = \int_0^1 \int_0^1 \mathbf{R}_{XY}(t_1, t_2) \psi_{k_1}^X(t_1) \psi_{k_2}^Y(t_2) dt_1 dt_2 \in \mathbb{R}^{p \times q}$.

Theorem 2 shows that $\mathbf{R}_{XY}(t_1, t_2)$ can be represented using the basis functions $\{\psi_k^X\}_{k \geq 1}$ and $\{\psi_k^Y\}_{k \geq 1}$. These bases capture the functional variations in the singular functions $\tilde{\mathbf{A}}_r^X$ and $\tilde{\mathbf{A}}_r^Y$, allowing $\mathbf{R}_{XY}(t_1, t_2)$ to be expanded on the tensor product basis $\{\psi_{k_1}^X(t_1) \psi_{k_2}^Y(t_2); k_1, k_2 \geq 1\}$. While similar approaches are used in functional and longitudinal analyses (Górecki et al., 2017, 2020; Hu and Yao, 2022; Lee et al., 2023), our method differs in that we do not pre-specify basis functions, for example by assuming data lie in known finite-dimensional spaces, but instead estimate them directly from the cross-covariance between \mathbf{X} and \mathbf{Y} .

To obtain the bases of \mathcal{H}_1 and \mathcal{H}_2 , we define the positive-definite kernels

$$H_X(t_1, t_2) := \text{tr}\{\mathbf{L}_X(t_1, t_2)\}/(pq) = \frac{1}{pq} \sum_{j=1}^p \sum_{m=1}^q \int_0^1 R_{jm}^{XY}(t_1, t) R_{jm}^{XY}(t_2, t) dt, \quad (4)$$

$$H_Y(t_1, t_2) := \text{tr}\{\mathbf{L}_Y(t_1, t_2)\}/(pq) = \frac{1}{pq} \sum_{j=1}^p \sum_{m=1}^q \int_0^1 R_{jm}^{XY}(t, t_1) R_{jm}^{XY}(t, t_2) dt, \quad (5)$$

where $R_{jm}^{XY}(t_1, t_2)$ is the (j, m) th element of $\mathbf{R}_{XY}(t_1, t_2)$. Here, H_X can be viewed as a marginal kernel of $R_{jm}^{XY}(t_1, t) R_{jm}^{XY}(t_2, t)$, aggregating over feature indices j, m and the time index t from \mathbf{Y} . It thus captures the variation in \mathbf{X} arising from these kernel products. Because $H_X(t_1, t_2)$ can also be written as $H_X(t_1, t_2) = \frac{1}{pq} \sum_{r=1}^{\infty} \lambda_r^2 \sum_{j=1}^p \tilde{\mathbf{A}}_{rj}^X(t_1) \tilde{\mathbf{A}}_{rj}^X(t_2)$ (since $\mathbf{L}_X(t_1, t_2) = \sum_{r=1}^{\infty} \lambda_r^2 \tilde{\mathbf{A}}_r^X(t_1) \{\tilde{\mathbf{A}}_r^X(t_2)\}^{\top}$), which aggregates all functional variation in the bases $\tilde{\mathbf{A}}_{rj}^X$ ($j = 1, \dots, p, r \geq 1$) for \mathcal{H}_1 , we can use $H_X(t_1, t_2)$ to extract functional bases for \mathcal{H}_1 , and similarly $H_Y(t_1, t_2)$ for \mathcal{H}_2 , as stated in the following theorem.

Theorem 3 (Extraction of Functional Bases). *Assume the conditions in Theorem 1 hold. Let the spectral decompositions of $H_X(t_1, t_2)$ and $H_Y(t_1, t_2)$ be*

$$H_X(t_1, t_2) = \sum_{k \geq 1} \zeta_k^X \tilde{\psi}_k^X(t_1) \tilde{\psi}_k^X(t_2), \quad H_Y(t_1, t_2) = \sum_{k \geq 1} \zeta_k^Y \tilde{\psi}_k^Y(t_1) \tilde{\psi}_k^Y(t_2),$$

where $\tilde{\psi}_k^X$ and $\tilde{\psi}_k^Y$ are the k th eigenfunctions with eigenvalues ζ_k^X and ζ_k^Y , respectively. Then, $\mathcal{H}_1 \subset \text{span}\{\tilde{\psi}_{k_1}^X : k_1 \geq 1\}$ and $\mathcal{H}_2 \subset \text{span}\{\tilde{\psi}_{k_2}^Y : k_2 \geq 1\}$. Define $\tilde{\Lambda}_{k_1, k_2}^{XY} = \int_0^1 \int_0^1 \mathbf{R}_{XY}(t_1, t_2) \tilde{\psi}_{k_1}^X(t_1) \tilde{\psi}_{k_2}^Y(t_2) dt_1 dt_2$, we have

$$\mathbf{R}_{XY}(t_1, t_2) = \sum_{k_1=1}^{\infty} \sum_{k_2=1}^{\infty} \tilde{\Lambda}_{k_1, k_2}^{XY} \tilde{\psi}_{k_1}^X(t_1) \tilde{\psi}_{k_2}^Y(t_2). \quad (6)$$

Theorem 3 shows that the bases of \mathcal{H}_1 and \mathcal{H}_2 can be obtained via the spectral decompositions of $H_X(t_1, t_2)$ and $H_Y(t_1, t_2)$, respectively.

Next, we will show that with these bases, the spectral decompositions of $\mathbf{L}_X(t_1, t_2)$ and $\mathbf{L}_Y(t_1, t_2)$ are transformed into the SVD of a matrix.

Truncated Approximation of \mathbf{R}_{XY} . Assuming $\{\tilde{\psi}_k^X : k \geq 1\}$ and $\{\tilde{\psi}_k^Y : k \geq 1\}$ have eigenvalues decaying with k , we can then approximate $\tilde{\mathbf{A}}_r^X$ and $\tilde{\mathbf{A}}_r^Y$ by working on a truncated version of (6) to approximate $\mathbf{R}_{XY}(t_1, t_2)$: $\mathbf{R}_{XY}(t_1, t_2) \approx \sum_{k_1=1}^{\kappa_X} \sum_{k_2=1}^{\kappa_Y} \tilde{\Lambda}_{k_1, k_2}^{XY} \tilde{\psi}_{k_1}^X(t_1) \tilde{\psi}_{k_2}^Y(t_2)$, where κ_X and κ_Y are finite numbers. Let $\mathbf{\Gamma}$ be a block matrix with the (k_1, k_2) th block as $\tilde{\Lambda}_{k_1, k_2}^{XY}$ for $k_1 = 1, \dots, \kappa_X$ and $k_2 = 1, \dots, \kappa_Y$. Assume the SVD of $\mathbf{\Gamma} \in \mathbb{R}^{p\kappa_X \times q\kappa_Y}$ is

$$\mathbf{\Gamma} = \sum_{r=1}^R \eta_r \cdot \mathbf{a}_r \mathbf{b}_r^\top, \quad (7)$$

where R is the rank of $\mathbf{\Gamma}$, and η_r , \mathbf{a}_r , and \mathbf{b}_r are the r th singular value/vectors of $\mathbf{\Gamma}$, respectively. Denote $\mathbf{a}_r = ((\mathbf{a}_r^{(1)})^\top, \dots, (\mathbf{a}_r^{(\kappa_X)})^\top)^\top \in \mathbb{R}^{p\kappa_X}$ and $\mathbf{b}_r = ((\mathbf{b}_r^{(1)})^\top, \dots, (\mathbf{b}_r^{(\kappa_Y)})^\top)^\top \in \mathbb{R}^{q\kappa_Y}$. The truncated approximation $\mathbf{R}_{XY}^{(\kappa_X, \kappa_Y)}(t_1, t_2) := \sum_{k_1=1}^{\kappa_X} \sum_{k_2=1}^{\kappa_Y} \tilde{\Lambda}_{k_1, k_2}^{XY} \tilde{\psi}_{k_1}^X(t_1) \tilde{\psi}_{k_2}^Y(t_2)$ can be rewritten as

$$\begin{aligned} \mathbf{R}_{XY}^{(\kappa_X, \kappa_Y)}(t_1, t_2) &= \sum_{r=1}^R \eta_r \cdot \left\{ \sum_{k_1=1}^{\kappa_X} \mathbf{a}_r^{(k_1)} \cdot \tilde{\psi}_{k_1}^X(t_1) \right\} \left\{ \sum_{k_2=1}^{\kappa_Y} \mathbf{b}_r^{(k_2)} \cdot \tilde{\psi}_{k_2}^Y(t_2) \right\}^\top \\ &:= \sum_{r=1}^R \eta_r \cdot \tilde{\mathbf{A}}_{r, \text{appr}}^X(t_1) \{ \tilde{\mathbf{A}}_{r, \text{appr}}^Y(t_2) \}^\top, \quad t_1, t_2 \in [0, 1]. \end{aligned} \quad (8)$$

This representation takes the same form as (2). Consequently, the decomposition of cross-covariance $\mathbf{R}_{XY}(t_1, t_2)$ is simplified into the SVD of matrix $\mathbf{\Gamma}$.

Note that the signs of $\tilde{\mathbf{A}}_r^X$ and $\tilde{\mathbf{A}}_r^Y$ are not identifiable. Without loss of generality, we align them with the signs of $\tilde{\mathbf{A}}_{r,\text{appr}}^X$ and $\tilde{\mathbf{A}}_{r,\text{appr}}^Y$, respectively, such that $\langle \tilde{\mathbf{A}}_r^X, \tilde{\mathbf{A}}_{r,\text{appr}}^X \rangle_p \geq 0$ and $\langle \tilde{\mathbf{A}}_r^Y, \tilde{\mathbf{A}}_{r,\text{appr}}^Y \rangle_q \geq 0$. The accuracy of $\tilde{\mathbf{A}}_{r,\text{appr}}^X$ and $\tilde{\mathbf{A}}_{r,\text{appr}}^Y$ then depends on the decay rates of the eigenvalues $\{\zeta_k^X, k > \kappa_X\}$ and $\{\zeta_k^Y, k > \kappa_Y\}$, as shown in the next theorem.

Theorem 4 (Perturbation Bound). *Assume the conditions in Theorem 1 hold. Suppose $\max_{1 \leq j \leq p, 1 \leq m \leq q} \int_0^1 \int_0^1 \{R_{jm}^{XY}(t, s)\}^2 dt ds$ is bounded by a constant, and that the singular values λ_r of $\mathbf{R}_{XY}(t_1, t_2)$ are distinct. Then,*

$$\max \left\{ \|\tilde{\mathbf{A}}_r^X - \tilde{\mathbf{A}}_{r,\text{appr}}^X\|_p, \|\tilde{\mathbf{A}}_r^Y - \tilde{\mathbf{A}}_{r,\text{appr}}^Y\|_q \right\} \leq \frac{C \cdot pq}{\inf_{r' \neq r} |\lambda_r^2 - \lambda_{r'}^2|} \sqrt{\sum_{k_1 > \kappa_X} \zeta_{k_1}^X + \sum_{k_2 > \kappa_Y} \zeta_{k_2}^Y},$$

where C is a constant independent of p, q, κ_X and κ_Y .

The rate in Theorem 4 indicates that the truncation levels κ_X and κ_Y should be chosen based on the decay behavior of the eigenvalues of $H_X(t_1, t_2)$ and $H_Y(t_1, t_2)$ to ensure the accuracy of approximated singular functions. This rate acts like a perturbation bound: $\sum_{k_1 > \kappa_X} \zeta_{k_1}^X + \sum_{k_2 > \kappa_Y} \zeta_{k_2}^Y$ quantifies the truncation perturbation, the pq factor reflects a dimension-averaged accumulation across the $p \times q$ coordinates, and the eigen-gap $\inf_{r' \neq r} |\lambda_r^2 - \lambda_{r'}^2|$ governs stability by amplifying the error when it is small.

3 Canonical Cross-Covariance Analysis on Observed Data

In this section, we consider the FACD between two longitudinally observed high-dimensional datasets. We assume that

$$\mathbf{x}_{ig} = \boldsymbol{\mu}_X(T_{ig}) + \boldsymbol{\varepsilon}_i^X(T_{ig}) + \boldsymbol{\tau}_{ig}^X, \quad i = 1, \dots, n, \quad g = 1, \dots, N_i^X, \quad (9)$$

$$\mathbf{y}_{ih} = \boldsymbol{\mu}_Y(T_{ih}) + \boldsymbol{\varepsilon}_i^Y(T_{ih}) + \boldsymbol{\tau}_{ih}^Y, \quad i = 1, \dots, n, \quad h = 1, \dots, N_i^Y, \quad (10)$$

where $\{\boldsymbol{\varepsilon}_i^X, \boldsymbol{\varepsilon}_i^Y\}$ are correlated components for subject i but are independent across different i 's, for $i = 1, \dots, n$; N_i^X and N_i^Y are the numbers of observed time points for the i th subject's

functions; $\{T_{ig}; g = 1, \dots, N_i^X\}$ and $\{T_{ih}; h = 1, \dots, N_i^Y\}$ are the observed time points for the two datasets that may vary across different subjects; $\boldsymbol{\tau}_{ig}^X := (\tau_{i1g}^X, \dots, \tau_{ipg}^X)^\top \in \mathbb{R}^p$ and $\boldsymbol{\tau}_{ih}^Y := (\tau_{i1h}^Y, \dots, \tau_{iqh}^Y)^\top \in \mathbb{R}^q$ are vectors of mean-zero noise terms that are uncorrelated with $\{\boldsymbol{\varepsilon}_i^Y, \boldsymbol{\varepsilon}_i^X\}$. These noise terms are independent across different subjects across the two datasets, but may be dependent across different features and times within the same dataset.

The goal is to estimate $\{\tilde{A}_{rj}^X; j = 1, \dots, p\}$ and $\{\tilde{A}_{rm}^Y; m = 1, \dots, q\}$ and their associated scores based on the data \mathbf{x}_{ig} s and \mathbf{y}_{ih} s.

3.1 Basis Function Estimation

To perform FACD, we first estimate the functional bases $\{\tilde{\psi}_{k_1}^X : k_1 = 1, \dots, \kappa_X\}$ and $\{\tilde{\psi}_{k_2}^Y : k_2 = 1, \dots, \kappa_Y\}$. We begin by introducing spline functional spaces. Let $\mathcal{B}_{L,Z}$ denote the L -dimensional B-spline space of order Z with equally spaced knots over \mathcal{T} , and let $\mathcal{B}_{L,Z} \otimes \mathcal{B}_{L,Z}$ be its tensor product space, consisting of bivariate spline functions on $\mathcal{T} \times \mathcal{T}$.

We first estimate the mean functions $\boldsymbol{\mu}_X$ and $\boldsymbol{\mu}_Y$ of \mathbf{X}_i and \mathbf{Y}_i from the observed data \mathbf{x}_{ig} and \mathbf{y}_{ih} . Let μ_j^X and x_{ijg} denote the j th component of $\boldsymbol{\mu}_X$ and the j th element of \mathbf{x}_{ig} , respectively, and define μ_m^Y and y_{imh} analogously for $\boldsymbol{\mu}_Y$ and \mathbf{y}_{ih} . Following [Hsing and Eubank \(2015\)](#) and [Xiao \(2020\)](#), we estimate μ_j^X and μ_m^Y via spline regression on the observations $\{x_{ijg}\}$ and $\{y_{imh}\}$ with respect to their observation times. For each j , we compute

$$\hat{\mu}_j^X := \arg \min_{f \in \mathcal{B}_{L_\mu, 4}} \frac{1}{n} \sum_{i=1}^n \frac{1}{N_i^X} \sum_{g=1}^{N_i^X} \{x_{ijg} - f(T_{ig})\}^2 + \nu_{\mu, j}^X \mathcal{L}(f),$$

where $\mathcal{B}_{L_\mu, 4}$ is the cubic spline space, $\mathcal{L}(\cdot)$ is a smoothness penalty, and $\nu_{\mu, j}^X$ is its tuning parameter. We define $\hat{\mu}_m^Y$ similarly and set $\hat{\boldsymbol{\mu}}_X = (\hat{\mu}_1^X, \dots, \hat{\mu}_p^X)^\top$ and $\hat{\boldsymbol{\mu}}_Y = (\hat{\mu}_1^Y, \dots, \hat{\mu}_q^Y)^\top$.

Next, we estimate the basis functions $\{\tilde{\psi}_{k_1}^X : k_1 = 1, \dots, \kappa_X\}$ and $\{\tilde{\psi}_{k_2}^Y : k_2 = 1, \dots, \kappa_Y\}$ given the estimated mean functions. Recall that the (j, m) th element of $\mathbf{R}_{XY}(t_1, t_2)$ is denoted by $R_{jm}^{XY}(t_1, t_2)$. Denote $G_{i,jm}^{XY}(T_{ig}, T_{ih}) := \{x_{ijg} - \hat{\mu}_j^X(T_{ig})\} \cdot \{y_{imh} - \hat{\mu}_m^Y(T_{ih})\}$, which is an empirical realization of $R_{jm}^{XY}(T_{ig}, T_{ih})$ for the i th subject. Define

$$U_i^X(T_{ig_1}, T_{ig_2}) := \frac{1}{pq} \sum_{j=1}^p \sum_{m=1}^q \frac{1}{N_i^Y} \sum_{h=1}^{N_i^Y} G_{i,jm}^{XY}(T_{ig_1}, T_{ih}) \cdot G_{i,jm}^{XY}(T_{ig_2}, T_{ih}),$$

which is considered an empirical realization of the aggregated kernel $H_X(T_{ig_1}, T_{ig_2}) = \frac{1}{pq} \sum_{j=1}^p \sum_{m=1}^q \int_0^1 R_{jm}^{XY}(t_1, t) R_{jm}^{XY}(t_2, t) dt$ for the i th subject. Using this, we estimate $H_X(t_1, t_2)$ via the bivariate spline regression

$$\hat{H}_X(\cdot, \cdot) := \arg \min_{f \in \mathcal{B}_{L_H, 4} \otimes \mathcal{B}_{L_H, 4}} \frac{1}{n} \sum_{i=1}^n \frac{1}{(N_i^X - 1) N_i^X} \sum_{1 \leq g_1 < g_2 \leq N_i^X} \{U_i^X(T_{ig_1}, T_{ig_2}) - f(T_{ig_1}, T_{ig_2})\}^2 + \nu_H^X \mathcal{L}(f),$$

where ν_H^X is a tuning parameter.

For $\hat{\mu}_j^X$ and $\hat{\mu}_m^Y$, we adopt the roughness penalty $\mathcal{L}(f) = \int_0^1 \{f^{(2)}(t)\}^2 dt$. For the kernels \hat{H}_X and \hat{H}_Y , we use the bivariate roughness penalty $\mathcal{L}(f) = \int_0^1 \int_0^1 \left[\left(\frac{\partial^2 f}{\partial t_1^2} \right)^2 + \left(\frac{\partial^2 f}{\partial t_2^2} \right)^2 \right] dt_1 dt_2$, which separately penalizes roughness in the t_1 and t_2 directions (Wood, 2006). Such spline smoothing approaches are widely used in functional data analysis (Hsing and Eubank, 2015; Xiao, 2020). Here, we select the tuning parameters for mean and kernel estimation by generalized cross-validation (GCV) (Gu, 2013).

After estimating $H_X(t_1, t_2)$, we perform spectral decomposition on $\hat{H}_X(t_1, t_2)$ to obtain $\hat{\zeta}_k^X$ and $\hat{\psi}_k^X$. The number of components κ_X can be selected based on the cumulative proportion of eigenvalues, $\sum_{k=1}^{\kappa_X} \hat{\zeta}_k^X / \int_0^1 \hat{H}_X(t, t) dt$, for example, when it exceeds a threshold such as 0.95. The same procedure applies to \hat{H}_Y to obtain $\hat{\psi}_k^Y$ and κ_Y for the second dataset \mathbf{Y}_i .

3.2 Estimation of Canonical Functional Loadings and Scores

In this subsection, we demonstrate the estimation procedure for the canonical functional loadings \mathbf{A}_r^X s and \mathbf{A}_r^Y s as well as their scores given the bases $\hat{\psi}_k^X$, $k \leq \kappa_X$, and $\hat{\psi}_k^Y$, $k \leq \kappa_Y$. Recall that $\Lambda_{k_1, k_2}^{XY} = \iint_0^1 \mathbf{R}_{XY}(t_1, t_2) \psi_{k_1}^X(t_1) \psi_{k_2}^Y(t_2) dt_1 dt_2$ according to Theorem 2. We denote $\mathbf{G}_i^{XY}(T_{ig}, T_{ih}) := (G_{i,jm}^{XY}(T_{ig}, T_{ih}))_{j=1, \dots, p, m=1, \dots, q} \in \mathbb{R}^{p \times q}$ and define

$$\hat{\Lambda}_{i, k_1, k_2}^{XY} := \frac{1}{N_i^X N_i^Y} \sum_{g=1}^{N_i^X} \sum_{h=1}^{N_i^Y} \mathbf{G}_i^{XY}(T_{ig}, T_{ih}) \hat{\psi}_{k_1}^X(T_{ig}) \hat{\psi}_{k_2}^Y(T_{ih}),$$

which is the empirical realization of Λ_{k_1, k_2}^{XY} for the i th subject. Subsequently, we estimate Λ_{k_1, k_2}^{XY} by $\hat{\Lambda}_{k_1, k_2}^{XY} = \sum_{i=1}^n \hat{\Lambda}_{i, k_1, k_2}^{XY} / n$.

In parallel with (7), define $\hat{\Gamma} \in \mathbb{R}^{p\kappa_X \times q\kappa_Y}$ as a block matrix whose (k_1, k_2) th block is $\hat{\Lambda}_{k_1, k_2}^{XY}$

for $k_1 = 1, \dots, \kappa_X$ and $k_2 = 1, \dots, \kappa_Y$. We perform matrix SVD on $\hat{\Gamma}$: $\hat{\Gamma} = \sum_{r=1}^R \hat{\eta}_r \hat{\mathbf{a}}_r \hat{\mathbf{b}}_r^\top$, where $\hat{\eta}_r$ is the r th singular value, $\hat{\mathbf{a}}_r = ((\hat{\mathbf{a}}_r^{(1)})^\top, \dots, (\hat{\mathbf{a}}_r^{(\kappa_X)})^\top)^\top \in \mathbb{R}^{p\kappa_X}$, and $\hat{\mathbf{b}}_r = ((\hat{\mathbf{b}}_r^{(1)})^\top, \dots, (\hat{\mathbf{b}}_r^{(\kappa_Y)})^\top)^\top \in \mathbb{R}^{q\kappa_Y}$ are the r th singular vectors. Based on (8), the estimated r th loadings are

$$\hat{\mathbf{A}}_r^X = \sum_{k=1}^{\kappa_X} \hat{\mathbf{a}}_r^{(k)} \cdot \hat{\psi}_k^X \quad \text{and} \quad \hat{\mathbf{A}}_r^Y = \sum_{k=1}^{\kappa_Y} \hat{\mathbf{b}}_r^{(k)} \cdot \hat{\psi}_k^Y. \quad (11)$$

In high-dimensional settings where p and q are large, we assume that only a small subset of features in \mathbf{X} and \mathbf{Y} contribute to their covariance. Specifically, we define

$$\mathcal{S}_X := \{j \in \{1, \dots, p\} : \|\tilde{A}_{rj}^X\| \neq 0 \text{ for some } r \geq 1\}, \quad (12)$$

$$\mathcal{S}_Y := \{m \in \{1, \dots, q\} : \|\tilde{A}_{rm}^Y\| \neq 0 \text{ for some } r \geq 1\}, \quad (13)$$

where \mathcal{S}_X and \mathcal{S}_Y are small subsets of $\{1, \dots, p\}$ and $\{1, \dots, q\}$, respectively. This sparsity assumption alleviates the curse of dimensionality and enhances interpretability by identifying key features linking two high-dimensional longitudinal datasets. Under this assumption, instead of directly applying SVD to $\hat{\Gamma}$, we solve

$$\begin{aligned} \{\hat{\mathbf{a}}_1, \hat{\mathbf{b}}_1\} = \arg \min_{\mathbf{a} \in \mathbb{R}^{p\kappa_X}, \mathbf{b} \in \mathbb{R}^{q\kappa_Y}} & \|\hat{\Gamma} - \mathbf{a}\mathbf{b}^\top\|_F^2 + \varrho_X \sum_{j=1}^p \|A_j^X\| + \varrho_Y \sum_{m=1}^q \|A_m^Y\| \\ & \text{subject to } \mathbf{a}^\top \mathbf{a} \leq 1, \mathbf{b}^\top \mathbf{b} \leq 1, \end{aligned} \quad (14)$$

where $(A_1^X, \dots, A_p^X)^\top = \mathbf{A}_1^X$ and $(A_1^Y, \dots, A_q^Y)^\top = \mathbf{A}_1^Y$ are constructed from (11), using \mathbf{a} and \mathbf{b} in place of $\hat{\mathbf{a}}_1$ and $\hat{\mathbf{b}}_1$, and ϱ_X, ϱ_Y are tuning parameters inducing sparsity in the functional loadings through Lasso-type penalties (Hastie et al., 2009). As ϱ_X and ϱ_Y increase, the norms of \hat{A}_j^X and \hat{A}_m^Y shrink toward zero, identifying important features.

It is worth noting that (14) is equivalent to

$$\begin{aligned} \min_{\mathbf{a} \in \mathbb{R}^{p\kappa_X}, \mathbf{b} \in \mathbb{R}^{q\kappa_Y}} & \|\hat{\Gamma} - \mathbf{a}\mathbf{b}^\top\|_F^2 + \varrho_X \sum_{j=1}^p \sqrt{\sum_{k=1}^{\kappa_X} (a_j^{(k)})^2} + \varrho_Y \sum_{m=1}^q \sqrt{\sum_{k=1}^{\kappa_Y} (b_m^{(k)})^2} \\ & \text{subject to } \mathbf{a}^\top \mathbf{a} \leq 1 \text{ and } \mathbf{b}^\top \mathbf{b} \leq 1, \end{aligned}$$

where $a_j^{(k)}$ or $b_m^{(k)}$ is the j th or m th element of $\mathbf{a}^{(k)}$ or $\mathbf{b}^{(k)}$. The penalty terms share the same form as group-Lasso penalties (Hastie et al., 2009), with each group corresponding to a feature. Therefore, we can employ the iterative matrix factorization algorithm as in Lin et al. (2013) to optimize (14) (see Part E.1 in Supplementary Materials for details).

After obtaining $\hat{\mathbf{a}}_1 = ((\hat{\mathbf{a}}_1^{(1)})^\top, \dots, (\hat{\mathbf{a}}_1^{(\kappa_X)})^\top)^\top$ and $\hat{\mathbf{b}}_1 = ((\hat{\mathbf{b}}_1^{(1)})^\top, \dots, (\hat{\mathbf{b}}_1^{(\kappa_Y)})^\top)^\top$ from (14) and $\hat{\mathbf{A}}_1^X$ and $\hat{\mathbf{A}}_1^Y$ from (11), we can iteratively proceed to $r > 1$. Specifically, once we obtain $\{\hat{\mathbf{a}}_r, \hat{\mathbf{b}}_r\}$ for $r \leq R$, we estimate the $(R+1)$ th singular vectors of $\hat{\Gamma}$ by replacing $\hat{\Gamma}$ in (14) with $\hat{\Gamma} - \sum_{r=1}^R \hat{\eta}_r \hat{\mathbf{a}}_r \hat{\mathbf{b}}_r^\top$, where $\hat{\eta}_r = \hat{\mathbf{a}}_r^\top \hat{\Gamma} \hat{\mathbf{b}}_r$. The r th functional loadings are then estimated using (11). In parallel with (3), the r th scores for the i th subject are estimated by

$$\hat{z}_{ir}^X := \sum_{j=1}^p \frac{1}{N_i^X} \sum_{g=1}^{N_i^X} \hat{A}_{rj}^X(T_{ig}) \{x_{ijg} - \hat{\mu}_j^X(T_{ig})\}, \quad \hat{z}_{ir}^Y := \sum_{m=1}^q \frac{1}{N_i^Y} \sum_{h=1}^{N_i^Y} \hat{A}_{rm}^Y(T_{ih}) \{y_{imh} - \hat{\mu}_m^Y(T_{ih})\}.$$

The entire procedure for estimating the first component is summarized in Algorithm 1.

The tuning parameters ϱ_X and ϱ_Y in (14) are selected separately for each component. Using the first component as an example, we split the n samples into 5 groups indexed by \mathcal{U}_g , $g = 1, \dots, 5$, with $\cup_{g=1}^5 \mathcal{U}_g = \{1, \dots, n\}$. Let $\hat{\mathbf{a}}_1^{(-g)}$ and $\hat{\mathbf{b}}_1^{(-g)}$ be the maximizers of (14) obtained by replacing $\hat{\Gamma}$ with $\frac{1}{n - |\mathcal{U}_g|} \sum_{i \notin \mathcal{U}_g} \hat{\Gamma}_i$, where $\hat{\Gamma}_i$ is a block matrix whose (k_1, k_2) th block is $\hat{\Lambda}_{i, k_1, k_2}^{XY}$, and $|\cdot|$ denotes set cardinality. The optimal ϱ_X and ϱ_Y are chosen to maximize $\sum_{g=1}^5 (\hat{\mathbf{a}}_1^{(-g)})^\top \left(\frac{1}{|\mathcal{U}_g|} \sum_{i \in \mathcal{U}_g} \hat{\Gamma}_i \right) \hat{\mathbf{b}}_1^{(-g)}$.

4 Statistical Consistency

In this section, we establish the statistical convergence of FACD loadings in high-dimensional settings where $p, q \gg n$. We assume the numbers of observed time points, $\{N_i^X : i = 1, \dots, n\}$ and $\{N_i^Y : i = 1, \dots, n\}$, are fixed positive integers. Let N_X and N_Y denote their respective sample averages, i.e., $N_X := n^{-1} \sum_{i=1}^n N_i^X$ and $N_Y := n^{-1} \sum_{i=1}^n N_i^Y$. We further assume that $\{\tau_{ijg}^X\}$, $\{\tau_{imh}^Y\}$, $\{T_{ig}\}$, $\{T_{ih}\}$, and $\{(\varepsilon_i^X, \varepsilon_i^Y)\}$ are mutually independent. Throughout, C and c denote generic positive constants independent of n, p, q, N_i^X, N_i^Y , possibly differing by context.

We further introduce the following assumptions.

Algorithm 1: FACD of high-dimensional longitudinal data

Input: Observed data $\{\mathbf{x}_{ig}; i = 1, \dots, n, g = 1, \dots, N_i^X\}$ and $\{\mathbf{y}_{ih}; i = 1, \dots, n, h = 1, \dots, N_i^Y\}$; rank R ; tuning parameters $\nu_{\mu,j}^X, j = 1, \dots, p, \nu_{\mu,m}^Y, m = 1, \dots, q, \nu_H^X, \nu_H^Y$, and ϱ_r^X, ϱ_r^Y .

Step 1: Estimation of mean functions.

$$\hat{\mu}_j^X = \arg \min_{f \in \mathcal{B}_{L_{\mu},4}} \frac{1}{n} \sum_{i=1}^n \frac{1}{N_i^X} \sum_{g=1}^{N_i^X} \{x_{ig} - f(T_{ig})\}^2 + \nu_{\mu,j}^X \int_0^1 \{f^{(2)}(t)\}^2 dt, \quad j = 1, \dots, p, \quad (15)$$

$$\hat{\mu}_m^Y = \arg \min_{f \in \mathcal{B}_{L_{\mu},4}} \frac{1}{n} \sum_{i=1}^n \frac{1}{N_i^Y} \sum_{h=1}^{N_i^Y} \{y_{ih} - f(T_{ih})\}^2 + \nu_{\mu,m}^Y \int_0^1 \{f^{(2)}(t)\}^2 dt, \quad m = 1, \dots, q. \quad (16)$$

For each i, j, m, g, h , compute $G_{i,jm}^{XY}(T_{ig}, T_{ih}) = \{x_{ig} - \hat{\mu}_j^X(T_{ig})\} \{y_{ih} - \hat{\mu}_m^Y(T_{ih})\}$.

Step 2: Estimation of H_X and H_Y .

$$\hat{H}_X = \arg \min_{f \in \mathcal{B}_{L_H,4} \otimes \mathcal{B}_{L_H,4}} \frac{1}{n} \sum_{i=1}^n \frac{1}{(N_i^X - 1)N_i^X} \sum_{1 \leq g_1 < g_2 \leq N_i^X} \{U_i^X(T_{ig_1}, T_{ig_2}) - f(T_{ig_1}, T_{ig_2})\}^2 + \nu_H^X \mathcal{L}(f), \quad (17)$$

$$\hat{H}_Y = \arg \min_{f \in \mathcal{B}_{L_H,4} \otimes \mathcal{B}_{L_H,4}} \frac{1}{n} \sum_{i=1}^n \frac{1}{(N_i^Y - 1)N_i^Y} \sum_{1 \leq h_1 < h_2 \leq N_i^Y} \{U_i^Y(T_{ih_1}, T_{ih_2}) - f(T_{ih_1}, T_{ih_2})\}^2 + \nu_H^Y \mathcal{L}(f), \quad (18)$$

where $U_i^X(T_{ig_1}, T_{ig_2}) = \frac{1}{pq} \sum_{j=1}^p \sum_{m=1}^q \frac{1}{N_i^Y} \sum_{h=1}^{N_i^Y} G_{i,jm}^{XY}(T_{ig_1}, T_{ih}) G_{i,jm}^{XY}(T_{ig_2}, T_{ih})$ and $U_i^Y(T_{ih_1}, T_{ih_2}) = \frac{1}{pq} \sum_{j=1}^p \sum_{m=1}^q \frac{1}{N_i^X} \sum_{g=1}^{N_i^X} G_{i,jm}^{XY}(T_{ig}, T_{ih_1}) G_{i,jm}^{XY}(T_{ig}, T_{ih_2})$, and $\mathcal{L}(f) = \int_0^1 \int_0^1 \left[\left(\frac{\partial^2 f}{\partial t_1^2} \right)^2 + \left(\frac{\partial^2 f}{\partial t_2^2} \right)^2 \right] dt_1 dt_2$.

Step 3: Estimation of functional bases. Perform spectral decomposition of $\hat{H}_X(t_1, t_2)$ and $\hat{H}_Y(t_1, t_2)$ to obtain eigenvalues $\hat{\zeta}_k^X, \hat{\zeta}_k^Y$ and eigenfunctions $\hat{\psi}_k^X, \hat{\psi}_k^Y$. Select κ_X and κ_Y such that $\sum_{k=1}^{\kappa_X} \hat{\zeta}_k^X / \int_0^1 \hat{H}_X(t, t) dt > 0.95$ and similarly for κ_Y .

Step 4: Estimation of cross-covariances. Define $\hat{\Gamma}$ as a block matrix whose (k_1, k_2) th block is $\hat{\Lambda}_{k_1, k_2}^{XY}$, where $\hat{\Lambda}_{k_1, k_2}^{XY} = \frac{1}{n} \sum_{i=1}^n \left\{ \frac{1}{N_i^X N_i^Y} \sum_{g=1}^{N_i^X} \sum_{h=1}^{N_i^Y} \mathbf{G}_i^{XY}(T_{ig}, T_{ih}) \hat{\psi}_{k_1}^X(T_{ig}) \hat{\psi}_{k_2}^Y(T_{ih}) \right\}$, with $\mathbf{G}_i^{XY}(T_{ig}, T_{ih}) = (G_{i,jm}^{XY}(T_{ig}, T_{ih}))_{1 \leq j \leq p, 1 \leq m \leq q}$.

Step 5: Iterative estimation of canonical components. For $r = 1, \dots, R$:

$$\{\hat{\mathbf{a}}_r, \hat{\mathbf{b}}_r\} = \arg \min_{\mathbf{a} \in \mathbb{R}^{p \kappa_X}, \mathbf{b} \in \mathbb{R}^{q \kappa_Y}} \|\hat{\Gamma} - \mathbf{a}\mathbf{b}^\top\|_F^2 + \varrho_r^X \sum_{j=1}^p \|A_{rj}^X\| + \varrho_r^Y \sum_{m=1}^q \|A_{rm}^Y\|, \text{ subject to } \mathbf{a}^\top \mathbf{a} \leq 1, \quad \mathbf{b}^\top \mathbf{b} \leq 1,$$

where $(A_{r1}^X, \dots, A_{rp}^X)^\top = \sum_{k=1}^{\kappa_X} \mathbf{a}^{(k)} \cdot \hat{\psi}_k^X$ and $(A_{r1}^Y, \dots, A_{rq}^Y)^\top = \sum_{k=1}^{\kappa_Y} \mathbf{b}^{(k)} \cdot \hat{\psi}_k^Y$ with $\mathbf{a} = ((\mathbf{a}^{(1)})^\top, \dots, (\mathbf{a}^{(\kappa_X)})^\top)^\top \in \mathbb{R}^{p \cdot \kappa_X}$ and $\mathbf{b} = ((\mathbf{b}^{(1)})^\top, \dots, (\mathbf{b}^{(\kappa_Y)})^\top)^\top \in \mathbb{R}^{q \cdot \kappa_Y}$.

Update $\hat{\Gamma} \leftarrow \hat{\Gamma} - \hat{\eta}_r \hat{\mathbf{a}}_r \hat{\mathbf{b}}_r^\top$, where $\hat{\eta}_r = \hat{\mathbf{a}}_r^\top \hat{\Gamma} \hat{\mathbf{b}}_r$.

Compute canonical functional loadings $\hat{\mathbf{A}}_r^X = \sum_{k=1}^{\kappa_X} \hat{\mathbf{a}}_r^{(k)} \hat{\psi}_k^X$ and $\hat{\mathbf{A}}_r^Y = \sum_{k=1}^{\kappa_Y} \hat{\mathbf{b}}_r^{(k)} \hat{\psi}_k^Y$. Canonical scores are $\hat{z}_{ir}^X = \sum_{j=1}^p \frac{1}{N_i^X} \sum_{g=1}^{N_i^X} \hat{A}_{rj}^X(T_{ig}) \{x_{ig} - \hat{\mu}_j^X(T_{ig})\}$ and $\hat{z}_{ir}^Y = \sum_{m=1}^q \frac{1}{N_i^Y} \sum_{h=1}^{N_i^Y} \hat{A}_{rm}^Y(T_{ih}) \{y_{ih} - \hat{\mu}_m^Y(T_{ih})\}$.

Output: $\hat{\mathbf{A}}_r^X, \hat{\mathbf{A}}_r^Y, \hat{z}_{ir}^X$, and \hat{z}_{ir}^Y , for $i = 1, \dots, n$.

End for.

Assumption 1. $\boldsymbol{\varepsilon}_i^X := (\varepsilon_{i1}^X, \dots, \varepsilon_{ip}^X)^\top$ and $\boldsymbol{\varepsilon}_i^Y := (\varepsilon_{i1}^Y, \dots, \varepsilon_{iq}^Y)^\top$ are independent and identically distributed across subjects i . In addition, $\max_{1 \leq j \leq p} \mathbb{E} \|\varepsilon_{ij}^X\|^8 \leq C$. Analogous conditions hold for ε_{im}^Y s.

Assumption 2. The noise τ_{ijg}^X and τ_{imh}^Y are mean-zero random variables that are independent across datasets and subjects. In addition, $\max_{1 \leq i \leq n, 1 \leq j \leq p, 1 \leq g \leq N_i^X} \mathbb{E}(\tau_{ijg}^X)^8 \leq C$ and $\sup_{1 \leq i \leq n, 1 \leq g_1 \neq g_2 \leq N_i^X} \sum_{j=1}^p \text{Corr}(\tau_{ijg_1}^X, \tau_{ijg_2}^X) \leq C\sqrt{p}$. Analogous conditions hold for τ_{imh}^Y s.

Assumption 3. The time points $\{T_{ig} : i = 1, \dots, n, g = 1, \dots, N_i^X\}$ satisfy that $\{T_{ig} : g = 1, \dots, N_i^X\}$ are independently drawn from a distribution function F , where F has a positive, bounded, and continuously differentiable density on $[0, 1]$. Analogous conditions hold for $\{T_{ih} : i = 1, \dots, n, h = 1, \dots, N_i^Y\}$.

Assumptions 1–2 regulate the uncertainty in the functional data and the noise. In particular, Assumption 2 requires the temporal correlations in τ_{ijg}^X and τ_{imh}^Y to grow no faster than the rate \sqrt{p} or \sqrt{q} , ensuring that the temporal dependence between the main signal $\boldsymbol{\varepsilon}_i^X$ and $\boldsymbol{\varepsilon}_i^Y$ can be separated from the noise. Assumption 3 is a common assumption on the observed time points for functional data (Hsing and Eubank, 2015; Xiao, 2020).

Assumption 4. For $l \geq 2$, the mean functions μ_j^X and μ_m^Y possess continuous derivatives of order l , satisfying $\sup_{1 \leq j \leq p, t \in \mathcal{T}} |\mu_j^X(t)| \leq C$ and $\sup_{1 \leq m \leq q, t \in \mathcal{T}} |\mu_m^Y(t)| \leq C$, and $\sup_{1 \leq j \leq p} \|(\mu_j^X)^{(l)}\| \leq C$ and $\sup_{1 \leq m \leq q} \|(\mu_m^Y)^{(l)}\| \leq C$. Moreover, $H_X(t_1, t_2)$ and $H_Y(t_1, t_2)$ are functions on $\mathcal{T} \times \mathcal{T}$ with continuous and bounded partial derivatives of total order l .

Assumption 4 introduces a smoothness requirement on the mean and aggregated cross-covariance functions of the functional data, which controls the error of $\hat{\mu}_j^X$ and $\hat{\mu}_m^Y$ and of \hat{H}_X and \hat{H}_Y as $p, q \rightarrow \infty$. In Part C of the Supplementary Materials, we introduce additional conditions for mean and covariance estimation. These conditions are standard in the functional data literature (Xiao, 2020).

As we implement the decomposition of $\mathbf{R}_{XY}(t_1, t_2)$ using the spectral decompositions of $H_X(t_1, t_2)$ and $H_Y(t_1, t_2)$, we require the following condition.

Assumption 5. The eigenfunctions $\{\tilde{\psi}_k^X : k \geq 1\}$ and $\{\tilde{\psi}_k^Y : k \geq 1\}$ of $H_X(t_1, t_2)$ and $H_Y(t_1, t_2)$ are uniformly bounded. Moreover, there exist constants $c, C > 0$ and $a > 1$ such

that the corresponding eigenvalues satisfy, for all $k \geq 1$, $C k^{-a} \geq \zeta_k^X \geq c(\zeta_{k+1}^X + k^{-(a+1)})$, $C k^{-a} \geq \zeta_k^Y \geq c(\zeta_{k+1}^Y + k^{-(a+1)})$.

Assumption 6. For $r \leq R$, the singular values $\{\lambda_r\}_{r \geq 1}$ of $\mathbf{R}_{XY}(t_1, t_2)$ satisfy $\lambda_R > 0$ and $\frac{\inf_{1 \leq r_1 \neq r_2 \leq R+1} |\lambda_{r_1}^2 - \lambda_{r_2}^2|}{pq} > C$.

Assumption 5 imposes polynomial decay rates on the eigenvalues of $H_X(t_1, t_2)$ and $H_Y(t_1, t_2)$ to control the error arising from their spectral decompositions, consistent with conditions in the literature (Hall and Horowitz, 2007). Assumption 6 introduces a singular-gap condition for the $\mathbb{R}^{p \times q}$ -valued kernel $\mathbf{R}_{XY}(t_1, t_2)$, ensuring the identifiability of its first R singular components. Here, the denominator pq averages out dimensional effects in the singular gap.

Assumption 7. Define $C_{\mu, X} = \sup_{f > 1, 1 \leq j \leq p, 1 \leq i \leq n, 1 \leq g \leq N_i^X} \frac{(\mathbb{E} |\mu_j^X(T_{ig}) - \hat{\mu}_j^X(T_{ig})|^f)^{1/f}}{\sqrt{f \cdot \mathbb{E}(\mu_j^X(T_{ig}) - \hat{\mu}_j^X(T_{ig}))^2}}$. We similarly define $C_{\mu, Y}$ and set $C_{\mu} = \max\{C_{\mu, X}, C_{\mu, Y}\}$. Define

$$C_{\Gamma} = \sup_{f > 2, 1 \leq j \leq p, 1 \leq m \leq q, k_1 \geq 1, k_2 \geq 1} \frac{(\mathbb{E} |[\tilde{\Lambda}_{k_1, k_2}^{XY} - \hat{\Lambda}_{k_1, k_2}^{XY}]_{j, m}|^f)^{1/f}}{f \cdot \sqrt{\mathbb{E}(([\tilde{\Lambda}_{k_1, k_2}^{XY} - \hat{\Lambda}_{k_1, k_2}^{XY}]_{j, m})^2)}},$$

where $[\cdot]_{j, m}$ denotes the (j, m) -th entry of a matrix. Let $s_X = |\mathcal{S}_X|$ and $s_Y = |\mathcal{S}_Y|$, where \mathcal{S}_X and \mathcal{S}_Y are defined in (12) and (13). Assume $s_X \leq C\sqrt{p}$ or $s_Y \leq C\sqrt{q}$, and as $n, p, q \rightarrow \infty$,

$$\sqrt{s_X} + \sqrt{s_Y} = o\left(\frac{n^{l/(2l+2)}}{C_{\mu} C_{\Gamma} \log(p+q)}\right).$$

The quantities C_{μ} and C_{Γ} quantify the tail behavior of the estimation errors for the means μ_j^X and μ_m^Y , and for the cross-covariance matrix Γ , respectively. With this, Assumption 7 imposes restrictions on the growth rates of the sparsity levels s_X and s_Y as $n, p, q \rightarrow \infty$, ensuring that the penalized SVD in (14) remains consistent.

Next, we analyze the estimation error of the functional loadings $\tilde{\mathbf{A}}_r^X$ and $\tilde{\mathbf{A}}_r^Y$. Since their signs are not identifiable, we align them such that $\langle \tilde{\mathbf{A}}_r^X, \hat{\mathbf{A}}_r^X \rangle_p \geq 0$ and $\langle \tilde{\mathbf{A}}_r^Y, \hat{\mathbf{A}}_r^Y \rangle_q \geq 0$.

Theorem 5. Suppose the conditions in Theorem 4 and Assumptions 1–7 hold together with the conditions in Part C of the Supplementary Materials. If the tuning parameters ν_H^X ,

ν_H^Y , ϱ^X , ϱ^Y , κ_X , and κ_Y satisfy the optimal orders given in Part D of the Supplementary Materials, then as $n, p, q \rightarrow \infty$,

$$\begin{aligned} & \max\{\|\tilde{\mathbf{A}}_r^X - \hat{\mathbf{A}}_r^X\|_p, \|\tilde{\mathbf{A}}_r^Y - \hat{\mathbf{A}}_r^Y\|_q\} \\ &= \mathcal{O}_p\left[\left\{C_\Gamma \cdot (Error_\mu + Error_H) \cdot \max\{\log(p), \log(q)\} \cdot \{\sqrt{s_X} + \sqrt{s_Y}\}\right\}^{\frac{a-1}{3a+3}}\right], \end{aligned}$$

where $Error_\mu = C_\mu \cdot \sqrt{\log(p+q)} \cdot \left\{(nN_X)^{-l/(2l+1)} + (nN_Y)^{-l/(2l+1)} + n^{-1/2}\right\}$ and $Error_H = (nN_X^2)^{-l/(2l+2)} + (nN_Y^2)^{-l/(2l+2)} + n^{-1/2}$.

Theorem 5 establishes the convergence rates of $\hat{\mathbf{A}}_r^X$ and $\hat{\mathbf{A}}_r^Y$ as $n, p, q \rightarrow \infty$. Here, $Error_\mu$ quantifies the error arising from high-dimensional mean estimation, whereas $Error_H$ represents the covariance estimation error when the true mean is given. Note that the rates in $Error_\mu$ and $Error_H$ depend on n , N_X , and N_Y . The terms $(nN_X)^{-l/(2l+1)}$, $(nN_Y)^{-l/(2l+1)}$, $(nN_X^2)^{-l/(2l+2)}$, and $(nN_Y^2)^{-l/(2l+2)}$ represent standard nonparametric convergence rates (Stone, 1982), while the $n^{-1/2}$ term reflects the parametric rate from independent functional samples. These rates all tend to 0 as n goes to infinity, regardless of the temporal sampling.

Note that $\hat{\mathbf{A}}_r^X$ and $\hat{\mathbf{A}}_r^Y$ are consistent as $n \rightarrow \infty$ under the sparsity Assumption 7, where the convergence rates depend on the ambient dimensions only through a $\log(p+q)$ factor as p and q increase. Consequently, the high dimensionality does not significantly affect the convergence of the functional loadings.

5 Simulation

5.1 Data Generation

For data generation, we consider the following models

$$\begin{aligned} x_{ijg} &= \sum_{r=1}^R A_{rj}^X(T_{ig}) z_{ir}^X + \tau_{ijg}^X, \quad i = 1, \dots, n, \quad j = 1, \dots, p, \quad g = 1, \dots, N_i^X, \\ y_{imh} &= \sum_{r=1}^R A_{rm}^Y(T_{ih}) z_{ir}^Y + \tau_{imh}^Y, \quad i = 1, \dots, n, \quad m = 1, \dots, q, \quad h = 1, \dots, N_i^Y, \end{aligned}$$

where The functional loadings A_{rj}^X and A_{rm}^Y are constructed as linear combinations of 10 basis functions, with the nonzero loadings concentrated in 10 variables of both datasets; $(z_{ir}^X, z_{ir}^Y)^\top$ denote the random scores, which are independent across subjects i and components r , and whose cross-covariance and correlation decay as r increases; τ_{ijg}^X s and τ_{imh}^Y s are correlated random noise terms. The noise terms τ_{ijg}^X and τ_{imh}^Y are generated in a way such that they are independent across different i and across the two datasets, but are dependent across different features and time points within the same dataset. The simulation of these components is detailed in Section E.2 of the Supplementary Materials. $\{T_{ig}; g = 1, \dots, N_i^X\}$ and $\{T_{ih}; h = 1, \dots, N_i^Y\}$, $i = 1, \dots, n$, are random time points sampled from $\text{Unif}([0, 1])$, with N_i^X s and N_i^Y s independently sampled from $\{5, 6, 7, 8\}$, and R is set to 20.

Under the above setting, $(z_{ir}^X, z_{ir}^Y)^\top$, $i = 1, \dots, n$, are the r th FACD and CCA scores from the two datasets, with the corresponding functional loadings being A_{rj}^X s and A_{rm}^Y s. Given x_{ijg} s and y_{imh} s, our goal is to estimate $(z_{ir}^X, z_{ir}^Y)^\top$, A_{rj}^X s, and A_{rm}^Y s.

5.2 Competing Methods and Evaluation Measures

For these tasks, we compare the proposed FACD with several existing CCA and dimension reduction methods: longitudinal canonical correlation analysis (LCCA; [Lee et al., 2023](#)), sparse canonical correlation analysis (SCCA; [Witten and Tibshirani, 2009](#)), multivariate functional principal component analysis (MFPCA; [Happ and Greven, 2018](#)), and a sparse variant of functional CCA ([Górecki et al., 2017](#)), referred to here as functional sparse canonical correlation analysis (FSCCA). Because some of these methods are not directly applicable to our simulated data, we made several necessary adaptations.

FSCCA is a modified version of functional CCA designed to accommodate the high-dimensional setting in our simulation. Specifically, we project the longitudinal data x_{ijg} and y_{imh} onto orthonormal cubic polynomial basis functions to obtain the projected data. Unlike [Górecki et al. \(2017\)](#), who applied CCA to the projected data to estimate scores and functional loadings, we employ GSCCA ([Lin et al., 2013](#)), which groups the projected variables of the same features during sparse estimation, thereby facilitating joint feature selection across datasets. SCCA also handles high-dimensional features but is limited to cross-sectional data; thus, we apply it to the subject-wise mean of longitudinal observations.

LCCA and MFPCA are implemented as originally proposed; however, LCCA uses linear bases to capture temporal patterns and lacks sparsity, while MFPCA is a unsupervised approach that independently extracts scores and loadings for each dataset.

We evaluate the performance of different methods using three criteria: (i) Estimation errors of functional loadings: $\sum_{j=1}^p \|A_{rj}^X - \hat{A}_{rj}^X\|^2$ and $\sum_{m=1}^q \|A_{rm}^Y - \hat{A}_{rm}^Y\|^2$, where \hat{A}_{rj}^X and \hat{A}_{rm}^Y are the estimated functional loadings from different methods; (ii) Variable selection errors: false positive rates $\frac{1}{p-10} \sum_{j=11}^p \mathbb{I}(\|\hat{A}_{rj}^X\| \neq 0) \times 100\%$ and $\frac{1}{q-10} \sum_{m=11}^q \mathbb{I}(\|\hat{A}_{rm}^Y\| \neq 0) \times 100\%$, and false negative rates $\frac{1}{10} \sum_{j=1}^{10} \mathbb{I}(\|\hat{A}_{rj}^X\| = 0) \times 100\%$ and $\frac{1}{10} \sum_{m=1}^{10} \mathbb{I}(\|\hat{A}_{rm}^Y\| = 0) \times 100\%$; (iii) Estimation accuracy of functional scores: $\widehat{\text{Cor}}(z_{ir}^X, \hat{z}_{ir}^X)$ and $\widehat{\text{Cor}}(z_{ir}^Y, \hat{z}_{ir}^Y)$, where \hat{z}_{ir}^X and \hat{z}_{ir}^Y are the estimated scores, and $\widehat{\text{Cor}}(\cdot, \cdot)$ denotes the empirical correlation.

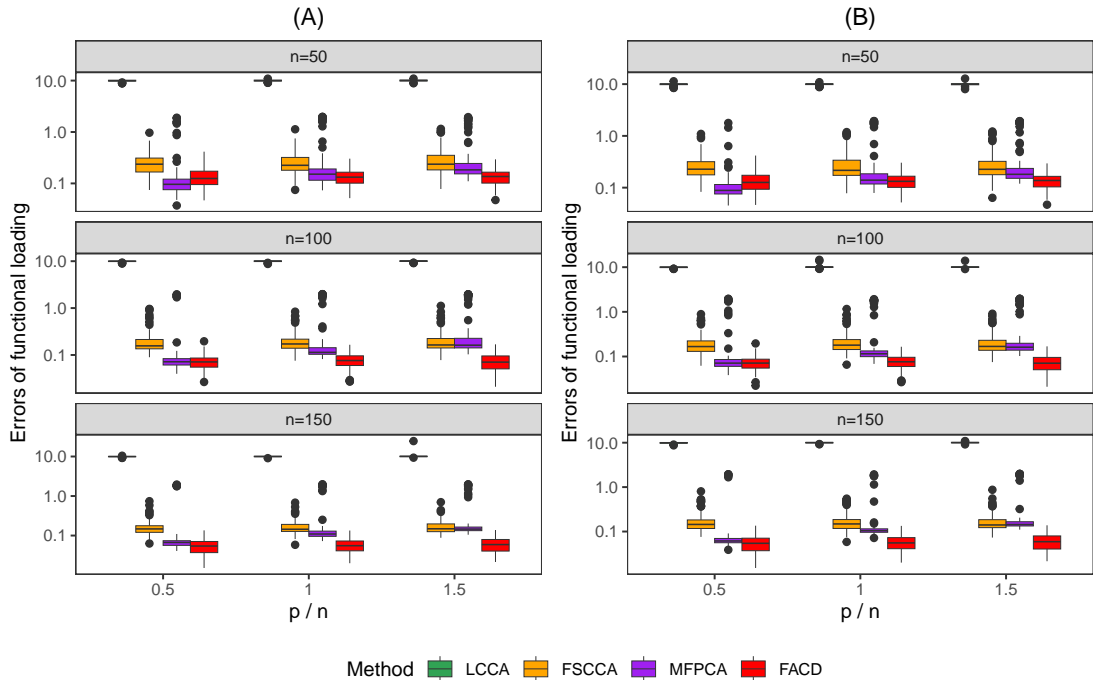


Figure 2: Boxplot of estimation errors for functional loadings from the first (Panel A) and second (Panel B) datasets.

5.3 Simulation Results

In this section, we examine settings with different combinations of n , p , and q , setting $p = q$ for simplicity. We conduct 300 simulations for each scenario and assess the estimation

performance of the first component. Figure 2 reports the estimation errors of functional loadings across methods. We observe that the performance of FACD is not sensitive to the dimensionality given that the true number of relevant variables is fixed. This phenomenon coincides with Theorem 5.

Overall, our proposed FACD consistently outperforms LCCA and FSCCA and achieves performance comparable to or better than MFPCA. The advantage of FACD over MFPCA becomes more evident as the p/n ratio increases, underscoring the benefit of exploiting cross-covariance information to enhance estimation in high-dimensional settings. In contrast, LCCA shows markedly higher errors, as it captures only linear longitudinal associations. Moreover, both LCCA and FSCCA rely on pre-specified basis functions, which may be inefficient for capturing the true underlying structure, leading to their inferior performance relative to FACD.

In Part E.3 of the Supplementary Materials, we further examine the estimation errors in the case of linear functional loadings, i.e., when A_{rj}^X and A_{rm}^Y are linear functions as assumed in LCCA. Under this setting, we find that FACD continues to outperform LCCA and FSCCA. This advantage stems from FACD’s ability to adaptively identify efficient longitudinal patterns while incorporating sparsity in the estimation of high-dimensional structures, capabilities not accommodated by LCCA or FSCCA.

Figure 3 shows the false positive and false negative rates for variable selection across the three methods capable of this task. FACD consistently attains markedly lower rates for both metrics. SCCA performs the worst, as it averages over all time points before applying CCA, leading to a substantial loss of temporal information. FSCCA improves upon SCCA by incorporating longitudinal signals but relies on pre-specified basis functions; when these bases are misaligned with the true temporal patterns, they capture inefficient signals and reduce selection accuracy. In particular, FSCCA significantly enlarges the false positive rate compared with FACD, suggesting that inefficient basis representations in FSCCA may introduce redundant and spurious cross-view associations that inflates weak effects into significant ones. In contrast, FACD employs data-adaptive bases that capture the true underlying longitudinal structure, resulting in more accurate variable selection.

Similar results are presented in Table 1 of the Supplementary Materials, which compares

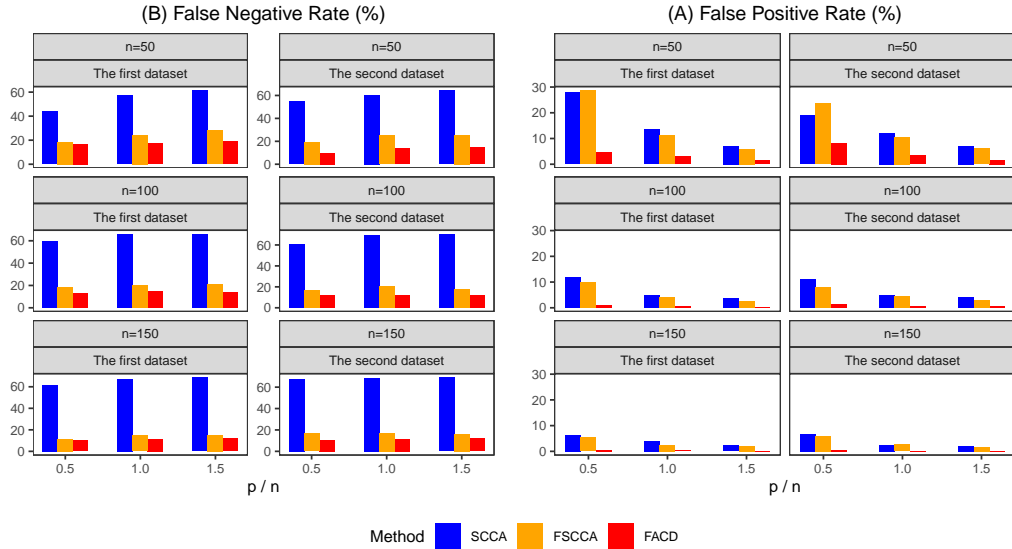


Figure 3: The false positive rates and false negative rates of variable selection.

the Pearson correlations between the estimated and true scores across methods. These results confirm that FACD most effectively recovers the top correlated structures between longitudinal datasets.

6 Data Analysis

To illustrate the utility of FACD, we analyze data from a longitudinal multi-omic study profiling blood molecules (Contreipois et al., 2020). Blood samples from 36 participants were collected at baseline and at 2, 15, 30, and 60 minutes post-exercise during a controlled session following overnight fasting. Plasma samples were analyzed by SWATH-MS for untargeted proteomics, immunoassays for targeted proteomics, LC-MS for untargeted metabolomics, and Lipidlyzer for semi-targeted lipidomics, capturing key dynamic molecular responses to acute physical activity. There are a small number of missing values at some time points that occur randomly, which are not aligned across subjects or across omic layers. Preprocessed data were obtained from <http://hmp2-data.stanford.edu/> and include 728, 710, 109, and 260 features for metabolites, lipids, targeted proteins, and untargeted proteins, respectively. We remove 54 metabolites due to low prevalence across samples. Untargeted protein markers

are combined with targeted protein markers. All features were log-transformed and standardized across subjects and time points before being analyzed by FACD for each pair of omics.

Given the high collinearity among lipid features, we group lipids into 17 classes according to structural and functional similarity (Table 2 in the Supplementary Materials). Within each group, principal component analysis was applied, and the top components explaining over 95% of the variance were retained as representative features. For instance, the first principal component of the cholesteryl ester (CE) group is denoted as “CE.pc.1,” with subsequent components named similarly. This procedure yielded 122 aggregated lipid features for FACD analysis (Table 3 in the Supplementary Materials). Further preprocessing details are provided in Section E.5, and illustrative examples of the processed data are shown in Figure 2 of the Supplementary Materials.

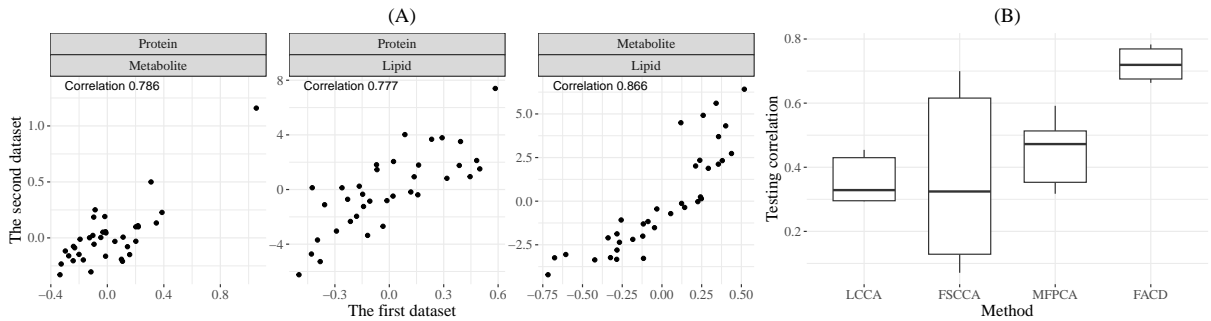


Figure 4: (A) The extracted first canonical scores of the participants between any two omics types of high-dimensional longitudinal data, with correlations calculated using the Pearson correlation coefficient. (B) Boxplot of Pearson correlations between the scores of proteome and metabolome for each testing fold.

Figure 4(A) displays the functional scores obtained from rank-one FACD applied to each pairwise combination of the three omics types. The selected tuning parameters (κ_X , κ_Y , ϱ_X , and ϱ_Y) for each paired dataset are reported in Table 4 of the Supplementary Materials. Notably, lipids and metabolites exhibit the strongest overall correlation (0.866), consistent with the integrative analysis of [Contreipois et al. \(2020\)](#), which found stronger cross-omic links between lipids and metabolites than with protein markers.

We further compare FACD with LCCA, FSCCA, and MFPCA in extracting correlations between the proteomic and metabolomic data. The data were divided into six folds, using

one fold for testing and the remaining five for training, with tuning parameters selected via five-fold cross-validation. Given the estimated loadings \hat{A}_{1j}^X and \hat{A}_{1m}^Y from the training data, the test-set scores for participant i were computed as $\hat{z}_{i1}^{X,\text{test}} = \sum_{j=1}^p \sum_{g=1}^{N_i^X} x_{ijg} \hat{A}_{1j}^X(T_{ig})/N_i^X$ and $\hat{z}_{i1}^{Y,\text{test}} = \sum_{m=1}^q \sum_{h=1}^{N_i^Y} y_{imh} \hat{A}_{1m}^Y(T_{ih})/N_i^Y$. We then computed the Pearson correlation between the two test-set scores. As shown in Figure 4(B), FACD consistently achieves the highest correlations, demonstrating a superior ability to capture key associations between the longitudinal datasets.

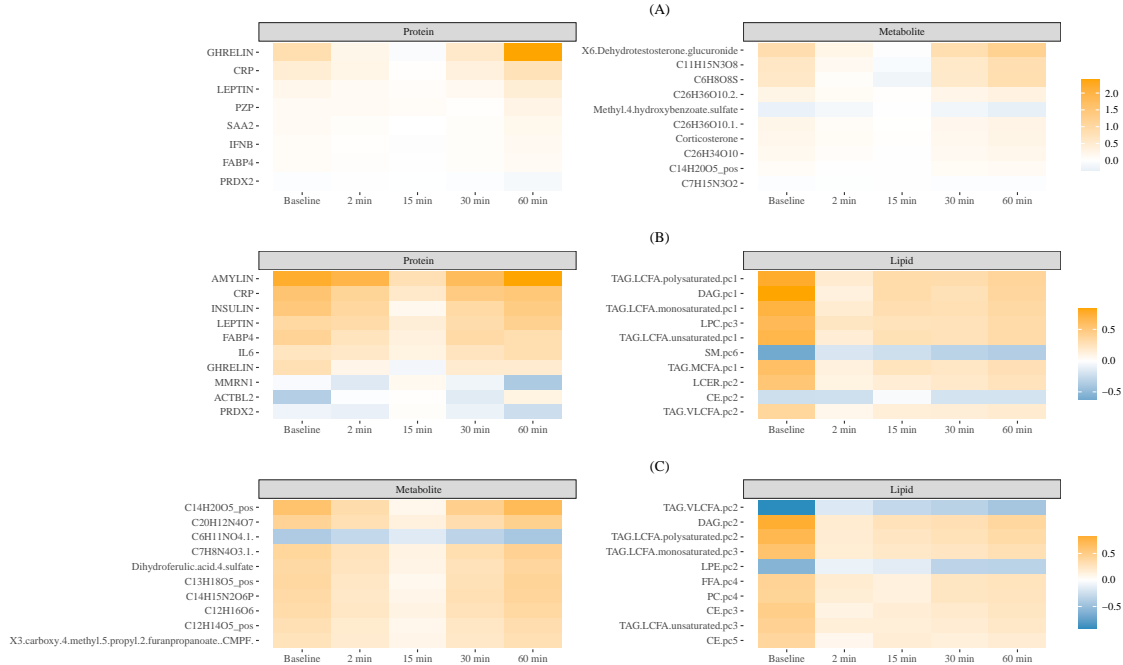


Figure 5: The estimated functional loadings between any two omics of high-dimensional longitudinal data. The signs of the functional loadings are determined such that their inner products with the constant function are positive. The signs of lipid features depend on the signs used in the principal component (PC) analysis, where the PC loadings are arranged to have a positive inner product with the constant vector. We only present the top 10 important features ranked by the L^2 norm of their functional loadings.

Figure 5 presents the estimated functional loadings of the top features selected by the first FACD component, capturing dominant longitudinal associations across omics. The sparsity penalties in optimization (14) resulted in the selection of 8 and 11 features between proteins and metabolites, 30 and 25 between proteins and lipids, and 24 and 29 between metabolites and lipids, respectively. These selected features are summarized in CSV files provided in the

Supplementary Materials.

The functional loadings reveal distinct temporal association patterns between omic layers. For instance, ghrelin, the “hunger hormone”, emerged as the leading protein marker associated with metabolites, with most associations occurring post-exercise. In contrast, lipid associations with other omics were primarily driven by baseline lipid levels, whereas protein and metabolite associations showed strong activity at both pre- and post-exercise time points. These distinct temporal patterns highlight asynchronous biological roles across omic layers and demonstrate the value of longitudinal multi-omic integration for uncovering dynamic molecular interactions.

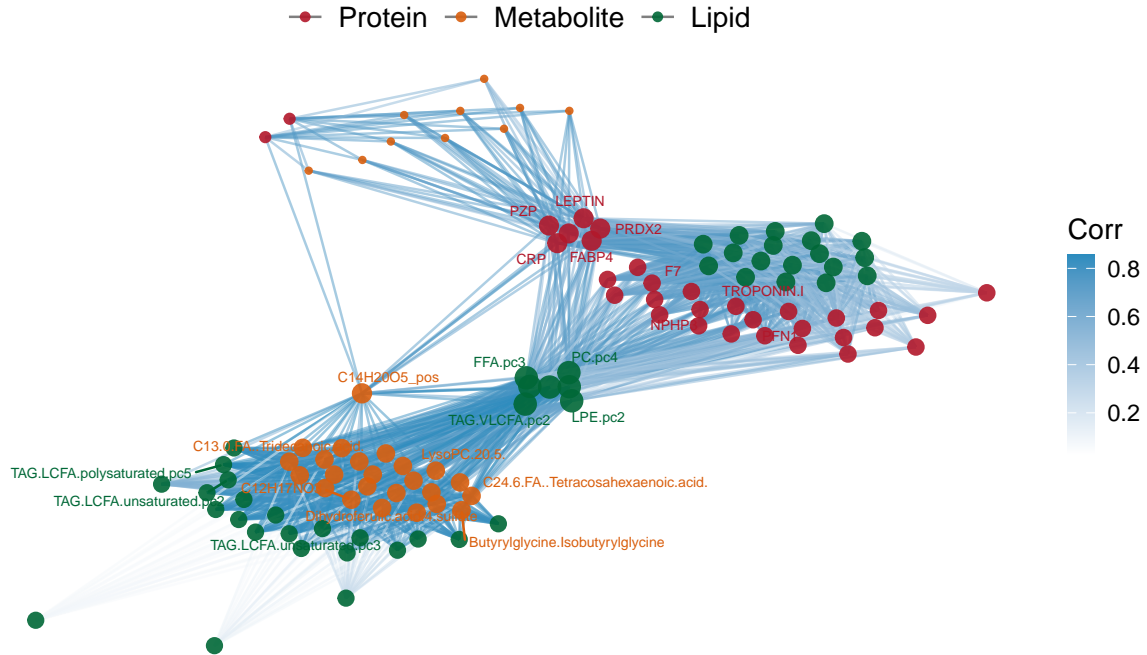


Figure 6: The time-integrated correlations between features from any two omics of high-dimensional longitudinal data, where larger node sizes indicate higher connectivity and deeper edge colors represent stronger correlations. We highlight the top 10 features with the largest number of connected edges for each omic. This network is plotted using the R package `ggraph` based on the correlation calculated by ρ_{jm} .

Figure 6 illustrates a network of predominant time-aggregated associations across omics, derived from rank-one FACD reconstructions. Specifically, for any two datasets, the reconstructions are defined as $\hat{X}_{ij}(\cdot) = \hat{A}_{1j}^X(\cdot) \hat{z}_{i1}^X$ and $\hat{Y}_{im}(\cdot) = \hat{A}_{1m}^Y(\cdot) \hat{z}_{i1}^Y$, and the correlation between the j th and m th features is computed as $\rho_{jm} := \frac{\frac{1}{n} \sum_{i=1}^n \langle \hat{X}_{ij}, \hat{Y}_{im} \rangle}{\sqrt{\frac{1}{n} \sum_{i=1}^n \|\hat{X}_{ij}\|^2} \cdot \sqrt{\frac{1}{n} \sum_{i=1}^n \|\hat{Y}_{im}\|^2}}$, quant-

tifying their overall temporal correlation based on the first FACD component. We find that the top protein markers identified exhibit clear and well-established biological relevance in the context of acute exercise. For instance, leptin and ghrelin are key hormonal regulators of energy balance and appetite; troponin I is a cardiac-specific contractile protein reflecting transient cardiac strain; FABP4 (fatty acid-binding protein 4) mediates fatty acid transport and energy mobilization; and CRP (C-reactive protein) is a marker of systemic inflammation elevated under physiological stress. Together, these proteins reveal coordinated metabolic, cardiovascular, and inflammatory adaptations to acute exercise, underscoring FACD’s ability to uncover biologically meaningful cross-omic relationships.

7 Discussion

In this article, we introduce the Functional-Aggregated Cross-covariance Decomposition (FACD), a novel framework for identifying key features and their longitudinal associations between paired high-dimensional datasets. At its core, FACD employs a functional-aggregation strategy that extracts data-adaptive bases from high-dimensional cross-covariances, enabling efficient decomposition of the cross-covariance structure via a tractable sparse singular value decomposition. We established theoretical guarantees for FACD, demonstrating statistical convergence in high-dimensional settings, and validated its empirical performance through extensive simulations. Finally, the application of FACD to longitudinal multi-omic data illustrates its potential to drive scientific discovery in biological research.

Overall, our approach shares the same spirit as functional partial least squares regression ([Beyaztas and Shang, 2020](#)), where a univariate functional outcome variable is regressed on multivariate functional predictors. The FACD framework has the potential to enhance such regression tasks by accommodating higher dimensionality in both predictors and outcomes, and by more effectively capturing the functional relationships between them through cross-covariance-informed, data-adaptive bases. We plan to explore this topic in future work.

References

Beyaztas, U. and Shang, H. L. (2020). On function-on-function regression: Partial least squares approach. *Environmental and Ecological Statistics*, 27(1):95–114.

Contrepois, K., Wu, S., Moneghetti, K. J., Hornburg, D., Ahadi, S., Tsai, M.-S., Metwally, A. A., Wei, E., Lee-McMullen, B., Quijada, J. V., et al. (2020). Molecular choreography of acute exercise. *Cell*, 181(5):1112–1130.

Diray-Arce, J., Fourati, S., Jayavelu, N. D., Patel, R., Maguire, C., Chang, A. C., Dandekar, R., Qi, J., Lee, B. H., van Zalm, P., et al. (2023). Multi-omic longitudinal study reveals immune correlates of clinical course among hospitalized covid-19 patients. *Cell Reports Medicine*, 4(6):101079.

Eubank, R. and Hsing, T. (2008). Canonical correlation for stochastic processes. *Stochastic Processes and their Applications*, 118(9):1634–1661.

Górecki, T., Krzysko, M., and Wołyński, W. (2017). Correlation analysis for multivariate functional data. *Data Science: Innovative Developments in Data Analysis and Clustering*, pages 243–258.

Górecki, T., Krzyśko, M., and Wołyński, W. (2020). Independence test and canonical correlation analysis based on the alignment between kernel matrices for multivariate functional data. *The Artificial Intelligence Review*, 53(1):475–499.

Gu, C. (2013). *Smoothing spline ANOVA models*, volume 297. Springer.

Hall, P. and Horowitz, J. L. (2007). Methodology and convergence rates for functional linear regression. *Annals of Statistics*, 35(1):70–91.

Han, Y., Liu, X., Jia, Q., Xu, J., Shi, J., Li, X., Xie, G., Zhao, X., and He, K. (2024). Longitudinal multi-omics analysis uncovers the altered landscape of gut microbiota and plasma metabolome in response to high altitude. *Microbiome*, 12(1):70.

Hao, X., Li, C., Yan, J., Yao, X., Risacher, S. L., Saykin, A. J., Shen, L., Zhang, D., and Initiative, A. D. N. (2017). Identification of associations between genotypes and longitudinal phenotypes via temporally-constrained group sparse canonical correlation analysis. *Bioinformatics*, 33(14):i341–i349.

Happ, C. and Greven, S. (2018). Multivariate functional principal component analysis for data observed on different (dimensional) domains. *Journal of the American Statistical Association*, 113(522):649–659.

Härdle, W. K., Simar, L., Härdle, W. K., and Simar, L. (2015). Canonical correlation analysis. *Applied multivariate statistical analysis*, pages 443–454.

Hastie, T., Tibshirani, R., Friedman, J. H., and Friedman, J. H. (2009). *The elements of statistical learning: data mining, inference, and prediction*, volume 2. Springer.

He, G., Müller, H.-G., and Wang, J.-L. (2003). Functional canonical analysis for square integrable stochastic processes. *Journal of Multivariate Analysis*, 85(1):54–77.

Hsing, T. and Eubank, R. (2015). *Theoretical foundations of functional data analysis, with an introduction to linear operators*, volume 997. John Wiley & Sons.

Hu, X. and Yao, F. (2022). Sparse functional principal component analysis in high dimensions. *Statistica Sinica*, 32(4):1939–1960.

Lee, S., Choi, J., Fang, Z., and Bowman, F. D. (2023). Longitudinal canonical correlation analysis. *Journal of the Royal Statistical Society Series C: Applied Statistics*, 72(3):587–607.

Lin, D., Zhang, J., Li, J., Calhoun, V. D., Deng, H.-W., and Wang, Y.-P. (2013). Group sparse canonical correlation analysis for genomic data integration. *BMC Bioinformatics*, 14(1):1–16.

MoTrPAC Study Group Primary authors, Amar, D., Gay, N. R., Jean-Beltran, P. M., Leads, M. W. G., et al. (2024). Temporal dynamics of the multi-omic response to endurance exercise training. *Nature*, 629(8010):174–183.

Ng, Q. X., Yau, C. E., Yaow, C. Y. L., Chong, R. I. H., Chong, N. Z.-Y., Teoh, S. E., Lim, Y. L., Soh, A. Y. S., Ng, W. K., and Thumboo, J. (2023). What has longitudinal ‘omics’ studies taught us about irritable bowel syndrome? a systematic review. *Metabolites*, 13(4):484.

Parkhomenko, E., Tritchler, D., and Beyene, J. (2009). Sparse canonical correlation analysis with application to genomic data integration. *Statistical Applications in Genetics and Molecular Biology*, 8(1):1–34.

Shin, H. and Lee, S. (2015). Canonical correlation analysis for irregularly and sparsely observed functional data. *Journal of Multivariate Analysis*, 134(C):1–18.

Stone, C. J. (1982). Optimal global rates of convergence for nonparametric regression. *The Annals of Statistics*, 10(4):1040–1053.

Tierney, B. T., Kim, J., Overbey, E. G., Ryon, K. A., Foox, J., Sierra, M. A., Bhattacharya, C., Damle, N., Najjar, D., Park, J., et al. (2024). Longitudinal multi-omics analysis of host microbiome architecture and immune responses during short-term spaceflight. *Nature Microbiology*, 9(7):1661–1675.

Witten, D. M. and Tibshirani, R. J. (2009). Extensions of sparse canonical correlation analysis with applications to genomic data. *Statistical Applications in Genetics and Molecular Biology*, 8(1):1–27.

Wood, S. N. (2006). Low-rank scale-invariant tensor product smooths for generalized additive mixed models. *Biometrics*, 62(4):1025–1036.

Xiao, L. (2020). Asymptotic properties of penalized splines for functional data. *Bernoulli*, 26(4):2847–2875.

Yang, W., Müller, H.-G., and Stadtmüller, U. (2011). Functional singular component analysis. *Journal of the Royal Statistical Society Series B: Statistical Methodology*, 73(3):303–324.

Zhou, W., Sailani, M. R., Contrepois, K., Zhou, Y., Ahadi, S., Leopold, S. R., Zhang, M. J., Rao, V., Avina, M., Mishra, T., et al. (2019). Longitudinal multi-omics of host–microbe dynamics in prediabetes. *Nature*, 569(7758):663–671.